ORIGINAL PAPER

Triple-source saddle-curve cone-beam photon counting CT image reconstruction: A simulation study

Lin Xin [a], **Weihai Zhuo** [a], **Qian Liu** [b,*], **Tianwu Xie** [a,c,*], **Habib Zaidi** [c,d,e,f]

[a] Institute of Radiation Medicine, Fudan University, Shanghai, China
[b] School of Biomedical Engineering, Hainan University, Haikou, China
[c] Division of Nuclear Medicine and Molecular Imaging, Geneva University Hospital, Geneva, Switzerland
[d] Geneva Neuroscience Center, Geneva University, Geneva, Switzerland
[e] Department of Nuclear Medicine and Molecular Imaging, University of Groningen, University Medical Center Groningen, Groningen, the Netherlands
[f] Department of Nuclear Medicine, University of Southern Denmark, Odense, Denmark

Received 19 June 2022; accepted 5 October 2022

Abstract

Purpose: The most common detector material in the PC CT system, cannot achieve the best performance at a relatively higher photon flux rate. In the reconstruction view, the most commonly used filtered back projection, is not able to provide sufficient reconstructed image quality in spectral computed tomography (CT). Developing a triple-source saddle-curve cone-beam photon counting CT image reconstruction method can improve the temporal resolution.
Methods: Triple-source saddle-curve cone-beam trajectory was rearranged into four trajectory sets for simulation and reconstruction. Projection images in different energy bins were simulated by forward projection and photon counting CT respond model simulation. After simulation, the object was reconstructed using Katsevich's theory after photon counts correction using the pseudo inverse of photon counting CT response matrix. The material decomposition can be performed based on images in different energy bins.
Results: Root mean square error (RMSE) and structural similarity index (SSIM) are calculated to quantify the image quality of reconstruction images. Compared with FDK images, the RMSE for the triple-source image was improved by 27%, 21%, 14%, 8%, and 6% for the reconstrued image of 20–33, 33–47, 47–58, 58–69, 69–80 keV energy bin. The SSIM was improved by 1.031%, 0.665%, 0.396%, 0.235%, 0.174% for corresponding energy bin. The decomposition image based on corrected images shows improved RMSE and SSIM, each by 33.861% and 0.345%. SSIM of corrected decomposition image of iodine reaches 99.415% of the original image.
Conclusions: A new Triple-source saddle-curve cone-beam PC CT image reconstruction method was developed in this work. The exact reconstruction of the triple-source saddle-curve improved both the image quality and temporal resolution.

Keywords: Triple-source; Saddle curve CT; Photon counting CT; Exact reconstruction; Simulation study

* Corresponding authors: Qian Liu, School of Biomedical Engineering, Hainan University, Haikou 570100, China. Tianwu Xie, Fudan University, Institute of Radiation Medicine, 2094 Xietu Road, Shanghai 200032, China.
E-mail addresses: qliu@hainanu.edu.cn (Q. Liu), tianwuxie@fudan.edu.cn (T. Xie).

Z Med Phys **34** (2024) 408–418
https://doi.org/10.1016/j.zemedi.2022.10.003
www.elsevier.com/locate/zemedi

1 Introduction

Since spectral computed tomography enables improved tissue contrast, it has been used to meet multiple diagnostic objectives [1]. In traditional dual-energy CT, the maximum number of separable tissues is three [2]. Capable of performing multiple tissue decomposition, photon counting computed tomography (PC CT) was developed [3]. PC CT can perform multi-energy spectral CT by detecting photons of various energy using the pulse height analyzing technique. The ability to quantify more than three materials can help optimize visualization of lesions, such as coronary stenosis [4], and virtual non-calcium images have improved diagnostic performance in coronary artery lumen [5]. Besides tissue decomposition, insight into other benefits brought by PC CT related to the image performance has been proved in previous studies, such as photon weighting technique, higher spatial resolution image and low patient dose [6].

Cadmium (zinc) telluride (CdTe or CZT) is the most common detector material in PCCT system [6]. However, for CdTe or CZT detectors, the comparatively high density of imperfection can give a rise to the possibility of break down or quantum efficiency degradation at high photon fluence rate, also refer to as polarization [7]. Higher photon flux rate also can cause photons interact within a short time period, resulting in count loss. Improved capabilities at high flux can be achieved in smaller detector [8] but increase charge sharing, which could result in compromised spectral performance [9], causing further degradation in material decomposing [10].

Superior spectral imaging generated by PCCT makes multi-contrast imaging possible, which is promising to exploit more spectral information especially in cardiovascular applications [11]. However, when considering cases of high/irregular heart rates or pediatric and emergent cases, reconstruction could be extremely difficult. Higher temporal resolution is required for these cases. When using single source CT, shorter acquisition time, which also means a higher photon fluence rate, could improve the temporal resolution but degrade the quality of spectral image as described above. Besides photon flux rate, the spectral tailing caused by charge sharing and two secondary peaks in the spectrum except for the photopeak, which is caused by K-fluorescence, can also result in distortion in spectrum information [6]. The correction for photon counts in different energy bins is also necessary for decomposition.

In the reconstruction view, traditional filtered back projection (FBP), is not able to provide sufficient reconstructed image quality in spectral cone-beam CT due to increased noises [12]. With a circular scan trajectory, there are more image artifacts further away from the mid-plan [13]. Sufficient and necessary conditions for exact reconstruction have been proposed in 1980s [14,15]. After the first exact and efficient reconstruction formula for helical cone-beam CT [16], exact reconstruction algorithms for both helical and saddle curve cone-beam CT have been studied [17,18]. For the multiple source saddle CT, the best temporal resolution is optimized only when using triple-source, which is three times better temporal resolution than with single-source saddle CT [19]. The exact reconstruction method was based on Katsevich's algorithm [20]. Dual source hybrid spectral micro-CT using an energy-integrating and a photon-counting detector have been used for the separation of iodine (I), gold (Au), gadolinium (Gd), and calcium (Ca) with improved RMSE (root mean square error) [21]. Comparing to an asymmetric dual-energy CT system, a symmetric triple-source system is superior in reconstruction for meeting the condition of exact reconstruction [22]. Triple-source CT has been proposed to improve the temporal resolution for application within cardiology. A lower flux could be achieved with the same or better temporal resolution when using triple-source CT. With an optimized temporal resolution, lower patient dose and scatter signal could be achieved by triple-source CT compared with multiple source CT (more than 3 sources).

Current developing PCCT uses single-source or dual-source with CZT or silicon detectors and a circle source trajectory [23–27]. To avoid pile-up, current technique chose to use PCDs that have smaller detector elements so that the PDCs can resolve the individual photons. However, smaller detector elements can cause increasing charge sharing. Despite the potential of triple-source saddle curve design in optimizing temporal resolution without increasing charge sharing, the application of the concept of triple-source saddle curve on PC CT has not been investigated yet. This paper presents the first triple-source saddle-curve cone-beam PC CT system simulation work to validate the feasibility of the system. Spectral correction matrix was calculated from Monte Carlo simulation and applied to explore the possibility of multiple energy bin spectral correction.

2 Material and method

2.1 Triple-source CT system

Three sources were symmetrically positioned along the circle, with a flat photon counting detector plane in the opposite position (Fig. 1). R, the distance between source and rotation axis, is 200 mm, which is also the same as D, the distance between the center of detector plane and rotation axis. A single detector plane contains 250 * 250 pixels with pixel sizes of 0.5 * 0.5 mm^2. The radius of field of interest was calculated as followed:

$$r = \mathrm{R} * \sin\left(\arctan\left(\frac{d}{2(\mathrm{R}+\mathrm{D})}\right)\right) \tag{1}$$

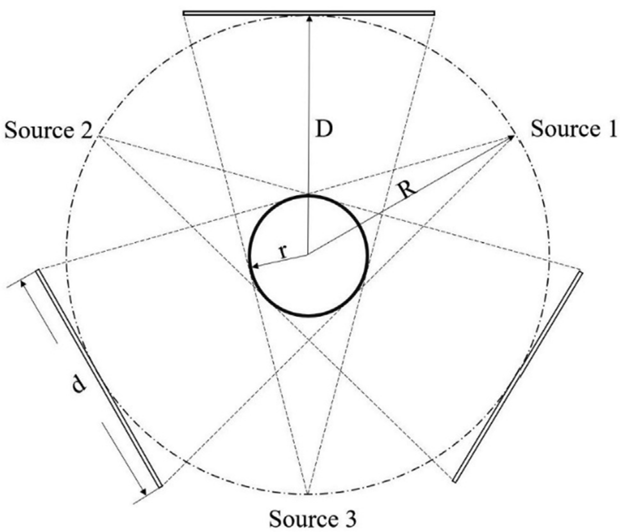

Figure 1. Triple-source photon counting CT system design.

where r stands for radius of field of interest, d stands for transaxial width of detector plane.

The detector area in this work is designed to sufficiently cover the rearranged projection lines. The projection lines were designed and rearranged as followed:

1. Three saddle curves are defined as:

$$C_i(\lambda) = \left(R\sin(\lambda), R\cos(\lambda), h\cos\left(2\lambda - \frac{2*(i-1)}{3}\pi\right)\right)$$
$$i = 1,2,3 \tag{2}$$

where λ is the angular parameter, and h is the pitch of each saddle, which is 20 mm in this work. 1080 projections for each saddle curves were generated.

2. When the lowest panel of field of interest (FOV) on axial direction (0, 0, -h) is needed to be exactly reconstructed, the saddle curves intersections at 0.5h are the piecewise for different saddle curves. When the highest projection on axial direction (0, 0, h) is needed to be exactly reconstructed, the intersections at -0.5h are the piecewise for different saddle curves. In one period of the saddles, four different rearranged curves can be generated from three original saddle curves (Fig. 2).

2.2 Simulation framework

The simulation process is based on the framework developed by Abadi et al. [28]. Concentric spheres phantom was used in this study to validate the system. The density and elemental composition for each material were defined based on NIST Standard Reference Database. Tube photon flux spectrum was generated using SPEKTR3.0 [29] with a tube voltage of 100kVp with mm Al and 0.5 mm Be filter.

The signal N_{pr} detected by each detector (i,j) at projection α at energy bin E was calculated by Beer-Lambert law:

$$N_{pr}(E,i,j,\alpha) = N_0(E,i,j,\alpha) \times \exp\left(-\sum_m \mu(E,m)l(i,j,\alpha,m)\right) \tag{3}$$

where N_0 is the numbers of photons, at energy E, at the source towards detector pixel (i, j) at projection α. μ is the linear attenuation coefficient of material m at energy E. l is the intersection length for material m with the ray detected by pixel (i, j) at projection α.

2.3 Photon CT Detector (PCD) model

When a photon reaches the center pixel, chances are that distortion in spectrum distortion only took place in the center and abutting pixels. To accelerate the simulation, we assumed the distortion spectrum was only recorded in the pixel that the photon reaches first. The actual photon CT detector count at each pixel was estimated as:

$$N(E,i,j,\alpha) = \sum\nolimits_u \sum\nolimits_v \times \sum_E \left(S(E,u,v,\alpha) + N_{pr}(E,u,v,\alpha)\right) R_{(u,v)}(E,i,j,t_n) \tag{10}$$

$R_{(u,v)}(E,i,j,t_n)$ is the probability of a photon at energy E reaching pixel (u,v) being detected at the energy threshold of t_n by pixel at (i,j). The probability expectation was estimated by the mean value of photon response at energy E detected by each energy bin by pixel at (i,j). The response was calculated by Monte Carlo simulation. The energy was divided into 5 energy bins by the threshold of 20, 33, 47, 58, 69, 80 keV. 10^8 events of simulation history were recorded. The total probability of a photon at energy E reaching pixel (u,v) being detected at the energy threshold of t_n by any pixel are shown in Fig. 3.

2.4 Photon counts correction

In order to redress the distortion in the energy response of PCD, the correction was performed as follow.

Step 1: Define the response matrix using Monte Carlo simulation result:

$$A = \begin{pmatrix} r_{1,1} & \cdots & r_{1,j} \\ \vdots & \ddots & \vdots \\ r_{i,1} & \cdots & r_{i,j} \end{pmatrix}$$

where $r_{i,j}$ is the photon response expectation of photon in energy bin j being detected at energy bin i.

Step 2: Let x being the original photon at energy bin i, and b being the signals for each energy bin i, and A^+ being the pseudo inverse of A. To solve the problem of

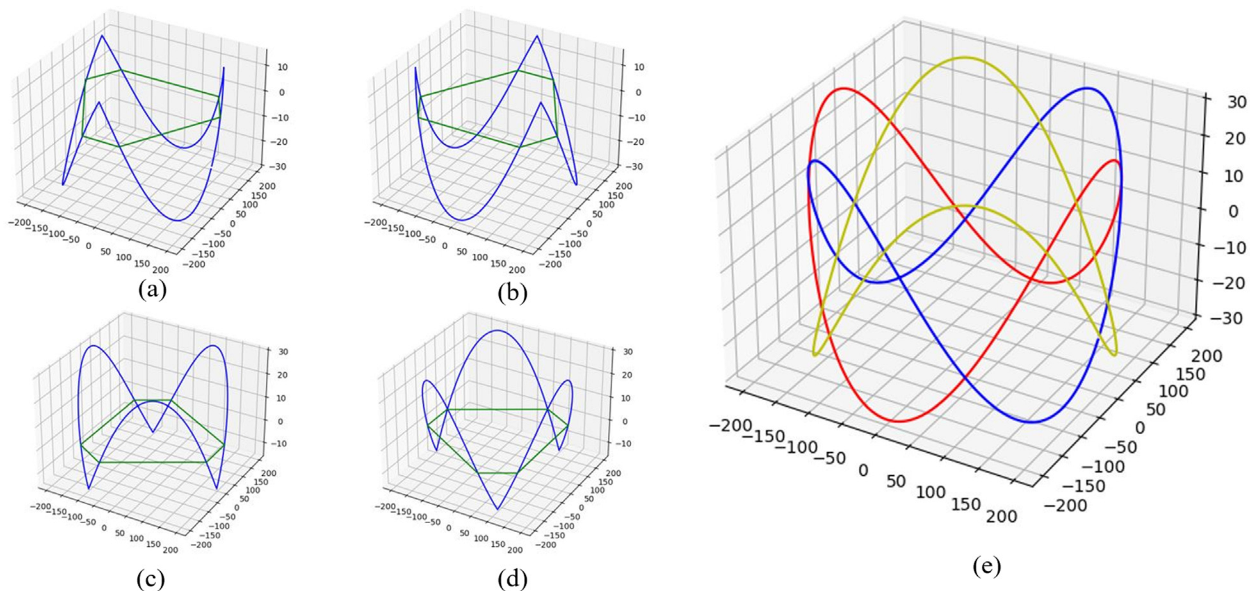

Figure 2. Four rearranged curves (a), (b), (c) and (d) and original three saddle curves (e), green line in the left figure shows the connection of intersections of saddle curves and the x–y plane. With highest projection on axial direction (0, 0, h) in (e), the saddle curves intersections at 0.5h in (a) and (b) while the saddle curves intersections at -0.5h in (c) and (d).

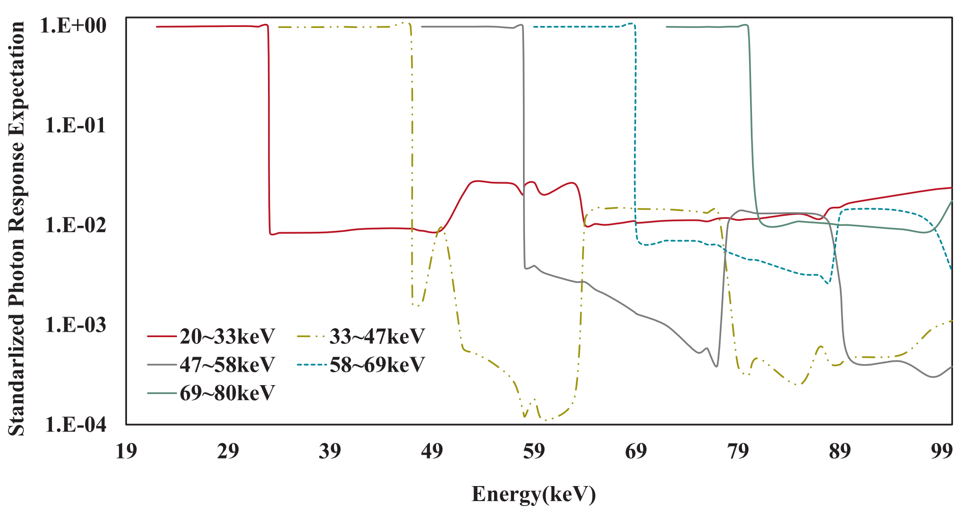

Figure 3. The total standard photon response expectation of photon E being detected at each energy bin by any pixel at the panel.

$\min_{x \in R} \|Ax - b\|$, then general least square solution can be implemented as $x = A^{+}b + (I_n - A^{+}A)y(y \in R^n)$ with the solution with minimum norm as $x = A^{+}b$. The solution with minimum norm was considered as corrected photon counts in this work.

2.5 Reconstruction algorithm

The reconstruction algorithm was based on the triple-source CT image reconstruction developed by Lu et al. [19]. The general formula of exact reconstruction of cone beam was derived by Yang et al. [30] as follows.

Let $\vec{x}$ be the point to be reconstructed, $\vec{e}$ be the filtering direction at each detector panel, $\vec{a}(\lambda)$ be the point on the scanning trajectory. Then,

$$\kappa\left(\vec{x}, \vec{e}, \lambda_i, \lambda_{i+1}\right) = -\frac{1}{2\pi^2} \int_{\lambda_i}^{\lambda_{i+1}} d\lambda \frac{1}{\|\vec{x} - \vec{a}(\lambda)\|} g_f\left(\lambda, \vec{x}, \vec{e}\right) \tag{11}$$

$$g_f(\lambda, \vec{x}, \vec{e}) = \int_{-\pi}^{\pi} d\gamma \frac{1}{\sin\gamma} \frac{\partial g\left(\lambda, \hat{\theta}(\lambda, \vec{x}, \vec{e}, \gamma)\right)}{\partial \lambda} \tag{12}$$

where

$$\hat{\theta}(\lambda, \vec{x}, \vec{e}, \gamma) = cos\gamma\hat{a}(\lambda, \vec{x}) + sin\gamma\hat{\beta}(\lambda, \vec{x}, \vec{e}) \tag{13}$$

$$\hat{a}(\lambda, \vec{x}) = \frac{\vec{x} - \vec{a}(\lambda)}{\|\vec{x} - \vec{a}(\lambda)\|} \tag{14}$$

$$\hat{\beta}(\lambda, \vec{x}, \vec{e}) = \frac{\vec{e} - (\vec{e} \cdot \hat{a}(\lambda, \vec{x}))\hat{a}(\lambda, \vec{x})}{\|\vec{e} - (\vec{e} \cdot \hat{a}(\lambda, \vec{x}))\hat{a}(\lambda, \vec{x})\|} \tag{15}$$

A pixel can be reconstructed as

$$f(\vec{x}) = \frac{1}{2}\kappa(\vec{x}, \vec{e}_{N,1}, \lambda_N, \lambda_1) + \frac{1}{2}\sum_{i=1}^{N-1}\kappa(\vec{x}, \vec{e}_{i,i+1}, \lambda_i, \lambda_{i+1}) N = 3, 4, 5 \cdots \tag{16}$$

where $\vec{e}_{i,j}$ are the filtering directions for projections between λ_i and λ_{i+1}. λ_i are the transection of the scanning trajectory and reconstruction plane. The reconstructed region is a convex polygon.

The algorithm can be implemented as:

Step 1: Rearrange the saddles.

Step 2: λ_i are the transection of the scanning trajectory and the x–y plane. The filter directions for rearranged curve are $\lambda_{i+1} - \lambda_i$. Then, filter direction were rearranged based on study by Lu et al. [19].

Step 3: Compute the derivative data for every projection g:

$$g_1(\lambda, i, j) = \left(\frac{\partial}{\partial \lambda} + \frac{D\prime(\lambda)i + i^2 + D^2(\lambda)}{D(\lambda)}\frac{\partial}{\partial i} + \frac{D\prime(\lambda)j + ij}{D(\lambda)}\frac{\partial}{\partial j}\right) g(\lambda, i, j) \tag{17}$$

The discrete partial derivatives were derived from derivatives of interpolation polynomial terms.

$$\frac{\partial}{\partial x} g_1(x_i) = \begin{cases} \frac{1}{2\Delta}[-3g(x_i) + 4g(x_{i+1}) - g(x_{i+2})], i = 0 \\ \frac{1}{2\Delta}[g(x_{i-2}) - 4g(x_{i-1}) + 3g(x_i)], i = N \\ \frac{1}{2\Delta}[-g(x_{i-1}) + g(x_{i+1})], otherwise \end{cases} \tag{18}$$

where N is the maximum value of i.

Step 4: Perform the filtration:

The filter directions were chosen based on study by Yang et al. [30]. Based on the filter directions, Hilbert transform process can be implemented as pre-weighting, forward height-base rearrangement, Hilbert transform and backward height-based rearrangement. The height $\hat{z}$ in the filtering process refers to the relative Height difference between the trajectory point and a point where the filtering plane intersects with the z-axis. The height-based filtering line on the panel can be described as:

$$j(Rsin\lambda \cdot e_x - Rcos\lambda \cdot e_y) = \hat{z}\left[((R + D)sin\lambda - icos\lambda)e_x - ((R + D)cos\lambda + isin\lambda)e_y\right] \tag{19}$$

The filtering process can be described as:

$$g_2(\lambda, i, j) = \frac{D(\lambda)}{\sqrt{D^2(\lambda) + i^2 + j^2}} g_1(\lambda, i, j) \tag{20}$$

$$g_3(\lambda, i, \hat{z}) = g_2(\lambda, i, j(i, \hat{z})) \tag{21}$$

where the rearrangement process was based on equation (19), and bilinear interpolation is used in this step,

$$g_4(\lambda, i, \hat{z}) = \int_{-\infty}^{\infty} di' h_H(i - i') g_3(\lambda, i, \hat{z}) \tag{22}$$

where h_H is the kernel of the Hilbert transform, with a discrete implementation as:

$$g_4(\lambda, i, \hat{z}) \approx \sum_{m'=-M}^{m-1} \frac{g_3(\lambda, i_{m'}, \hat{z})\Delta i}{i_{m'} - i_m} + \sum_{m'=m+1}^{M} \frac{g_3(\lambda, i_{m'}, \hat{z})\Delta i}{i_{m'} - i_m} \tag{23}$$

where -M<m'<M,

$$g_5(\lambda, i, j) = g_4(\lambda, i, \hat{z}(i, j)) \tag{24}$$

$$g_f^{Filtered}(\lambda, i, j) = \frac{\sqrt{D^2(\lambda) + i^2 + j^2}}{D(\lambda)} g_5(\lambda, i, j) \tag{25}$$

Step 5: Back projection were performed as:

$$f(\vec{x}) = -\frac{1}{4\pi}\int_{\lambda_s}^{\lambda_s + 2\pi} d\lambda \frac{1}{\|\vec{x} - \vec{a}(\lambda)\|} g_f^{Filtered}(\lambda, i, j) \tag{26}$$

2.6 Material decomposition

In traditional dual-energy CT, beam hardening effect cannot be fully eliminated. Decomposition images based on reconstruction images were not fully accurate. For PC CT, the beam hardening effect can be further eliminated based on more detailed spectral information. Therefore, decomposition based on reconstruction images was applied in this paper. For dual-energy CT, often then decomposition is performed using water and iodine as reference materials, by solving the equations:

$$\begin{aligned} \mu_{(\vec{x})}(E_{high}) &= \rho_{water}(\vec{x}) \cdot \mu_{water}(E_{high}) + \rho_{iodine}(\vec{x}) \cdot \mu_{iodine}(E_{high}) \\ \mu_{(\vec{x})}(E_{low}) &= \rho_{water}(\vec{x}) \cdot \mu_{water}(E_{low}) + \rho_{iodine}(\vec{x}) \cdot \mu_{iodine}(E_{low}) \end{aligned} \tag{27}$$

To exploit the spectral information detected by PCD, 5 energy bins were used to record the photon energy reaching the detector panel. For chosen materials model, the reconstruction images of energy bin E_j are linear characterized by basic materials as:

$$\mu_{(\vec{x})}(E_j) = \sum_{i=1}^{N} a_i(\vec{x}) \cdot \mu_i(E_j), subjectto \sum_{i=1}^{N} a_i(\vec{x}) = 1 \tag{28}$$

The decomposition coefficient in space can be solved by:

$$\begin{bmatrix} \mu(\vec{x})(E_1) \\ \vdots \\ \mu(\vec{x})(E_j) \end{bmatrix} = \begin{bmatrix} \mu_1(E_1) & \cdots & \mu_n(E_1) \\ \vdots & \ddots & \vdots \\ \mu_1(E_j) & \cdots & \mu_n(E_j) \end{bmatrix} \begin{bmatrix} a_{(1)}(\vec{x}) \\ \vdots \\ a_{(n)}(\vec{x}) \end{bmatrix},$$

$$subjectto \sum_{i=1}^{N} a_i(\vec{x}) = 1 \tag{29}$$

The pseudo inverse of basic material attenuation coefficient matrix was used for decomposition. The minimum norm of solution was applied in this work. The energy bin selection was based on the specific composition needs.

3 Result

3.1 Reconstruction algorithm

The accuracy of the reconstruction algorithm was testified by using simulating images without scattered signals and PCD response simulation. FDK reconstruction method were also used for reconstruction, applying hamming filtering. A phantom consisting of concentric spheres with different materials was used to validate the reconstruction algorithm quantitively. The phantom consists of six concentric spheres of skeleton, 15 mg/cc I solution, lung, soft tissue, water and adipose from inner layer to outer layer. The image shows there are more image artifacts further away from the mid-plan for FDK method (Fig. 4). The attenuation coefficient in energy bin 20-33keV was used to simulate the projection and algorithm validation. For a full cycle of triple-source projection, half of the plane in the middle can be constructed four times, and two times for other panels. The temporal resolution was three times as circular single curve FDK reconstruction algorithm. In order to quantify the quality of reconstruction images, the root mean square error (RMSE) can be used:

$$RMSE = \frac{\sqrt{\sum_{i=1}^{n}\sum_{j=1}^{n}\sum_{k=1}^{n}\left(u_{i,j,k} - r_{i,j,k}\right)^2}}{n^2} \tag{30}$$

where n is the pixel number of the image and u and r are the reconstructed and real image. To further evaluate the image quality in the view of human visual perception, structural similarity index (SSIM) was also calculated to quantify the visibility differences between reconstrued images and real images based on known characteristic of the human visual system (HVS) [31].

$$SSIM(u,r) = \frac{(2\mu_u\mu_r + \varepsilon)(2\sigma_{ur} + \varepsilon)}{\left(\mu_u^2 + \mu_r^2 + \varepsilon\right)\left(\sigma_u^2 + \sigma_r^2 + \varepsilon\right)} \tag{31}$$

where μ_u and μ_r are mean value of reconstructed images and real images, and σ_{ur}, σ_u and σ_r are covariance and standard deviations of reconstructed images and real images. $\epsilon = 10^{-8}$ in the equation. Comparing with FDK images, the RMSE for triple-source image was improved by 27%, 21%, 14%, 8% and 6% for reconstrued image of 20–33, 33–47, 47–58, 58–69, 69–80 keV energy bin. The SSIM was improved by 1.031%,0.665%,0.396%,0.235%,0.174% for corresponding energy bin. The contrast information was more contained in the low-energy image. Therefore, an exact reconstruction image improved the image quality more significantly in low-energy bin. The result shows exact reconstruction of spectral information can help improve the contrast of the image, so that an improved diagnostic performance can be achieved.

To show the performance of the reconstruction method in more imaging tasks, a mouse phantom was used to show the accuracy of the reconstruction algorithm. The image of 58–69 keV energy bin was shown in Fig. 5. The reconstruction algorithm of this work shows greater accuracy compared with FDK reconstruction method considering a mouse phantom. Details in the mouse phantom were lost in the images reconstructed using FDK method. Such loss is less significant in the reconstruction image of this work.

3.2 Photon counts correction

In CdTe/CZT and Si detectors, spectral distortion caused by charge sharing and K-fluorescence [10], which is measured by Monte Carlo simulation in this work, can be partially corrected by pseudo inverse of PCD response matrix. Compared with the image without correction, the reconstruction image with correction shows improved RMSE and SSIM (Table 1). The correction was not fully accurate especially for material with high attenuation coefficient, such as skeleton tissue, which can further cause error in decomposition (Fig. 6). The distortion PCD response relatively caused the largest error in energy bin 20–33 keV. For energy bins over 33 keV, the distortion is almost neglectable for image reconstruction. The higher the energy widows, the smaller the error is. The image also shows artifacts close to the center of skeletal tissue. Fig. 7 shows that skeleton has relatively more significant drop in attenuation coefficient from 20–33 keV energy bin to the rest, which leads to larger differences in photon numbers reaching the detector panel in different bins. With fewer photons in 20–33 keV energy bin, the artifacts caused by the distortion of spectrum are more significant. In the middle of phantom, thicker material of bone was passed through by X-ray, leading to a more significant underestimation in attenuation coefficient.

3.3 Decomposition

A phantom consisting of six concentric spheres of Iodine-water resolution of different concentrations was used to validate the decomposition method. Water, iodine, skeleton and air were chosen as basic materials to perform decomposition. The decomposition image based on corrected images shows

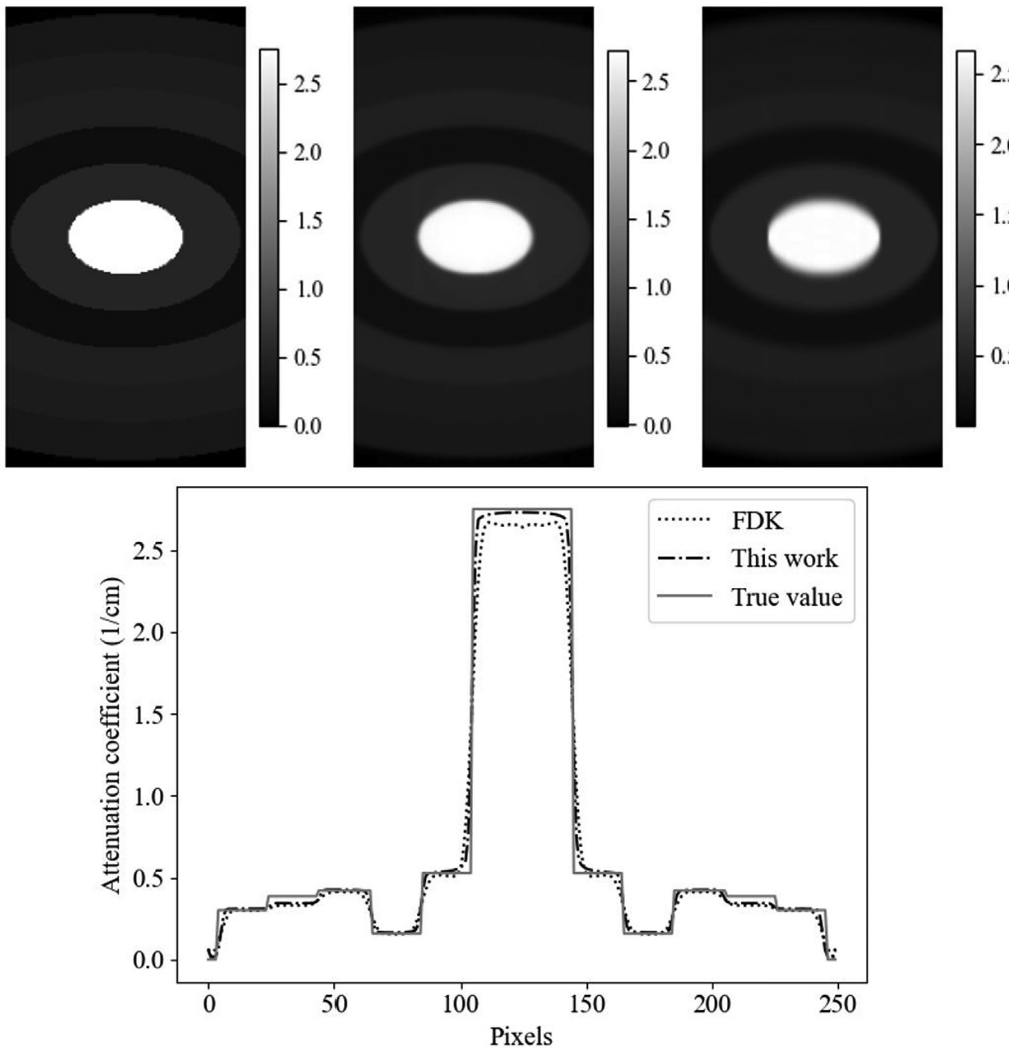

Figure 4. The original phantom (upper left), the reconstruction image in this work (using the first 1/3 of projections) (upper middle), reconstruction image using FDK method (upper right) and its profile along the central line.

improved RMSE and SSIM, each by 33.861% and 0.345%. SSIM of corrected decomposition image of I reaches 99.415% of the original image. A higher concentration of iodine volume mass fraction, which leads to higher attenuation coefficient, shows less relative error in the decomposition image (Fig. 8). When the concentration was relatively high, the correction improved the quality of the reconstructed attenuation image and decomposition image more significantly, especially when the volume mass fraction was above 0.015 mg/cc.

Virtual non-calcium images can improve diagnostic performance in coronary artery lumen. Decomposition for water, iodine, and calcium-containing tissue are of great clinical use. The distortion of spectral response of PCD could underestimate the attenuation coefficient of skeleton in the lower energy windows. This error could further introduce an artifact in the decomposition of iodine and skeleton (Fig. 9), which is similar to the previous study [32]. However, usually calcified tissue contains little iodine when considering human tissue. It is easy to eliminate the artifact by simply subtracting the image of calcified tissue in order to obtain non-calcium images. For tissue with rather low differences in attenuation coefficient in different energy windows, such as water, the artifact was not significant as calcified tissue.

4 Discussion and conclusion

A new Triple-source saddle-curve cone-beam photon counting CT image reconstruction method was developed in this work. Exact reconstruction of triple-source saddle-curve CT improved both the image quality and temporal res-

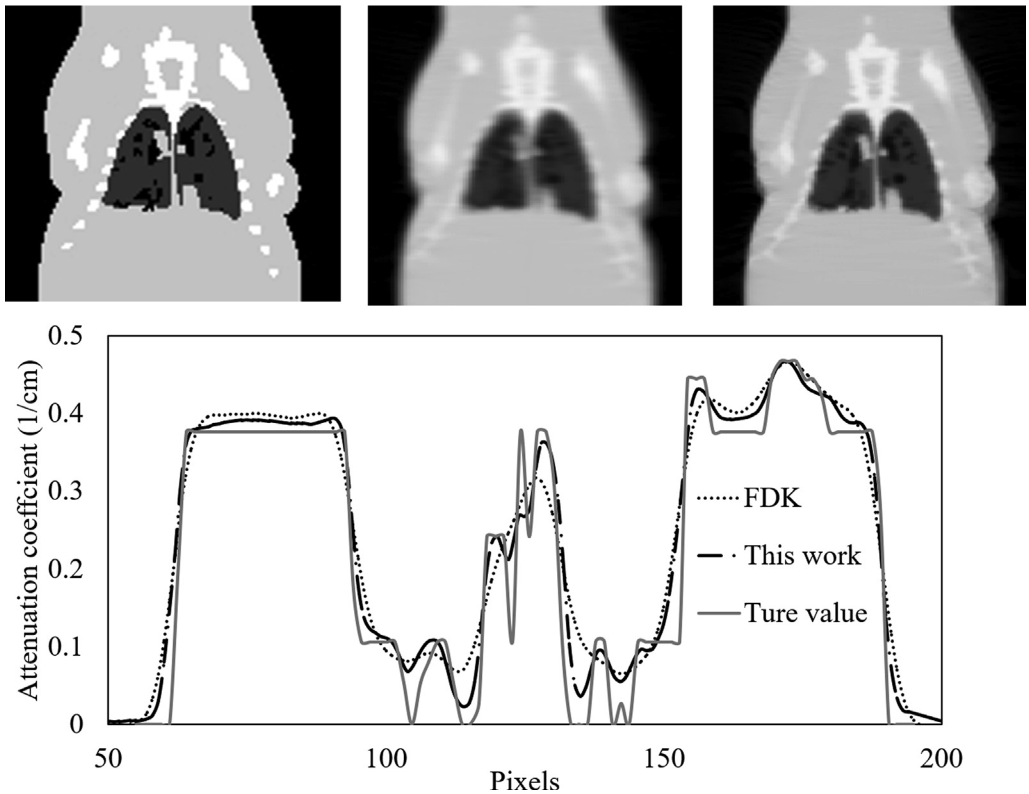

Figure 5. The original mouse phantom (upper left), the reconstruction image in this work (using the first 1/3 of projections) (upper middle), reconstruction image using FDK method (upper right) and its profile along the central line.

Table 1
Relative image quality index comparing with reconstructed image without scatter and distortion respond of PCD.

Energy bin (keV)	Relative RMSE uncorrected	Relative RMSE corrected	Relative SSIM uncorrected	Relative SSIM corrected
20–33	2.5229	1.0787	0.9500	0.9972
33–47	1.0268	1.0126	0.9992	0.9996
47–58	1.0046	1.0036	0.9998	0.9999
58–69	0.9881	0.9879	1.0003	1.0003
69–80	0.9857	0.9857	1.0003	1.0003

olution, comparing with image reconstructed with FDK method. The PCD response correction was applied to give an improved reconstruction performance in attenuation coefficient, therefore in the decomposition image.

Compared with the traditional saddle-curve triple-source system, PCCT can further exploit the high temporal resolution of the multiple-source system. Unlike helical multiple source system [17], the multiple source saddle curve system has a temporal resolution proportional to $\frac{2N+1}{N}$, which reaches maximum value when N = 3 [19]. Iterative algorithm has been developed for reconstruction problem in cone-beam CT [33]. However, the computational cost was still high compared with back projection methods. The detector area in this work had to sufficiently cover the rearranged projection lines, which also set limitations on the axial length of field of interest (FOV). To apply this system on clinical practice, a much larger and more complicated detector panel had to be redesigned.

The system in this simulation work only applied small FOV in order to accommodate the need for micro-CT system construction in future work. Therefore, the scatter simulation can be significantly underestimated for a much larger system with a wider detector panel.

In a dual-energy CT system, the intensity for cross scatter was equivalent or larger comparing to forward scatter depending on the size of the phantom [34]. Our results confirmed their findings because of the small phantom size. The

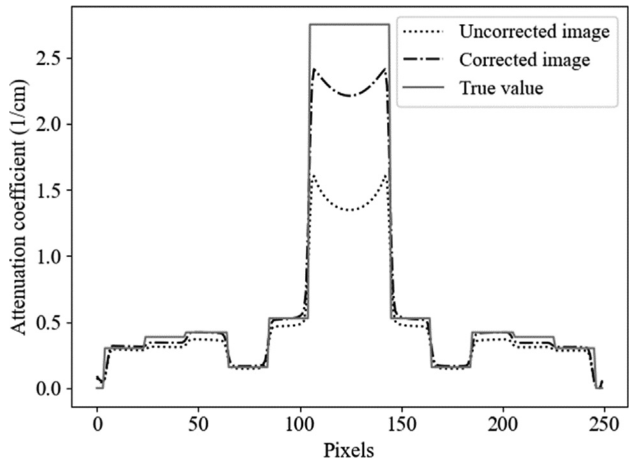

Figure 6. A profile line in the middle of the original phantom, the reconstruction image in this work (using the first 1/3 of projections) and reconstruction image using FDK method.

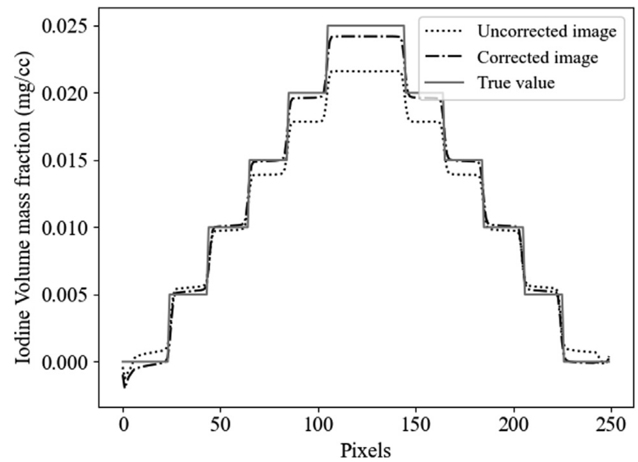

Figure 8. Image of Iodine Volume mass fraction

mean intensity for cross scatter of triple-source was 1.139 times of forward scatter. However, to accelerate the simulating of the scatter signal, the total scatter signal was considered as proportional to forward scatter, which is not precisely accurate. Further studies should be done to investigate the effect of cross scatter signals.

Compared with previous PCCT projection simulation work, the beam hardening effect was considered in a different method by calculating the attenuated X-ray passing the material at every energy level. In this way, the beam-hardening effect is more accurately estimated.

This work does not discuss the effect of scattered signal. Further work will be done to investigate the effect of scattered image.

Research showed that the appropriate spectrum can help reduce the distortion in PCD response [6]. The distortion in PCD was the most significant in the lower energy window, especially in 20–33 keV in this work. In dual-energy CT, an additional attenuation is measured at a second energy bin based on K-edge energy subtraction technique, allowing the differentiation of the calcified tissue and iodine [1]. 20–33 keV Energy bin was set to optimize the extracted K-edge signal for multi-energy imaging. To suppress the distortion, a correction method has been proposed by this work. It helped to accurately quantify the mass volume fraction of iodine. However, the method shows defects as it is shown in the last section. The photon flux rate was considered low enough, so the pile-up pulse was not considered in this work. More research should be done to investigate the

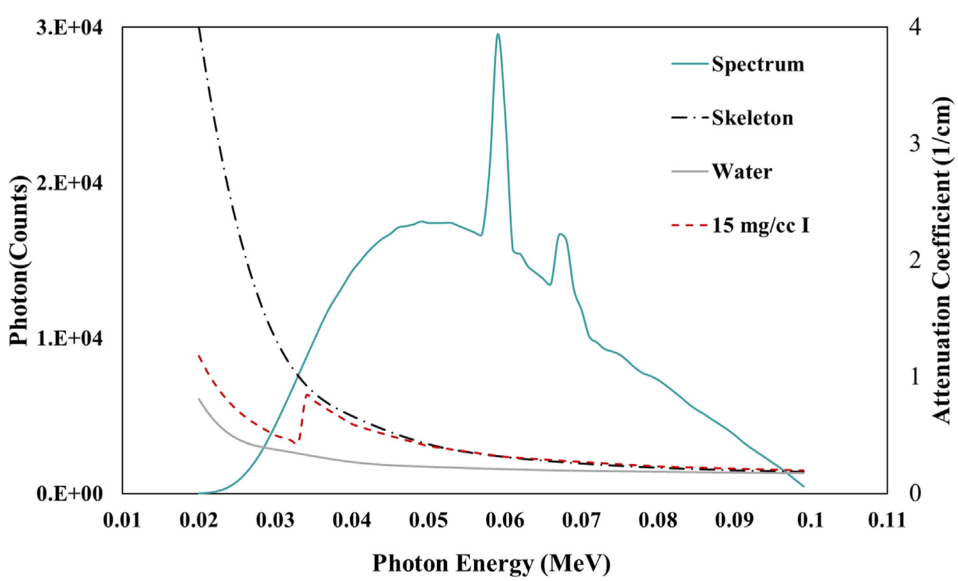

Figure 7. Attenuation coefficient for skeleton, water, 15mg/cc I solution and X-ray spectrum

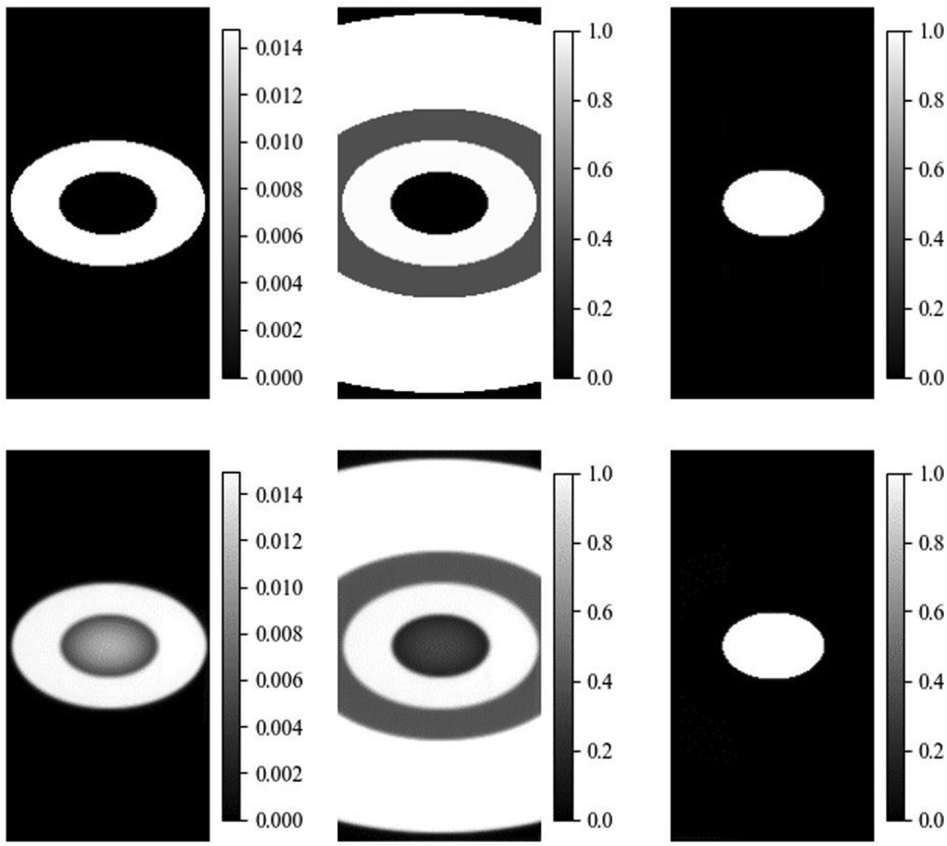

Figure 9. Iodine (left), water (middle), and skeleton (right) mass volume fraction after decomposition (corrected images), with true images in the first row and simulation images on the second row.

potential of further suppressing the artifact and investigate the effect of pulse pile-up. One of the most important means was to apply appropriate tube voltage and filter for an adjusted spectrum. To improve the quality of the K-edge decomposition imaging, optimizing the energy bins is another choice. Several energy window selection methods have been proposed in previous studies [35]. Further studies will be done to investigate the energy bin choices for triple-source CT.

Declaration of Competing Interest

The authors declare that they have no known competing financial interests or personal relationships that could have appeared to influence the work reported in this paper.

Acknowledgments

This study was supported by the start-up grant from Fudan University to T. X., the Key Laboratory of Biomedical Engineering of Hainan Province under Opening Foundation 2022001, Swiss National Science Foundation under grant SNFN 320030_176052, Qatar national research fund (NPRP10-0126-170263), National Natural Science Foundation of China (32227801).

References

[1] McCollough CH, Leng S, Yu L, Fletcher JG. Dual- and Multi-Energy CT: Principles, Technical Approaches, and Clinical Applications. Radiology 2015;276:637–653.

[2] Liu X, Yu L, Primak AN, McCollough CH. Quantitative imaging of element composition and mass fraction using dual-energy CT: Three-material decomposition. Med Phys 2009;36:1602–1609.

[3] Leng S, Zhou W, Yu Z, Halaweish A, Krauss B, Schmidt B, et al. Spectral performance of a whole-body research photon counting detector CT: quantitative accuracy in derived image sets. Phys Med Biol 2017;62:7216–7232.

[4] Stehli J, Clerc OF, Fuchs TA, Possner M, Gräni C, Benz DC, et al. Impact of monochromatic coronary computed tomography angiography from single-source dual-energy CT on coronary stenosis quantification. J Cardiovasc Comput Tomogr 2016;10:135–140.

[5] Yunaga H, Ohta Y, Kaetsu Y, Kitao S, Watanabe T, Furuse Y, et al. Diagnostic performance of calcification-suppressed coronary CT angiography using rapid kilovolt-switching dual-energy CT. Eur Radiol 2017;27:2794–2801.

[6] Danielsson M, Persson M, Sjölin M. Photon-counting x-ray detectors for CT. Phys Med Biol 2021;66:03tr1.

[7] Bale DS, Szeles C. Nature of polarization in wide-bandgap semiconductor detectors under high-flux irradiation: Application to semi-insulating Cd1−xZnxTe. Phys Rev B 2008;77:035205.

[8] Kappler S, Henning A, Krauss B, Schoeck F, Stierstorfer K, Weidinger T, et al. Multi-energy performance of a research prototype CT scanner with small-pixel counting detector. In: Nishikawa RM, Whiting BR, Hoeschen C, editors. Medical Imaging 2013: Physics of Medical Imaging2013.

[9] Hsieh SS, Rajbhandary PL, Pelc NJ. Spectral resolution and high-flux capability tradeoffs in CdTe detectors for clinical CT. Med Phys 2018;45:1433–1443.

[10] Xu C, Danielsson M, Bornefalk H. Evaluation of Energy Loss and Charge Sharing in Cadmium Telluride Detectors for Photon-Counting Computed Tomography. Nucl Sci IEEE Trans 2011;58:614–625.

[11] Kwan AC, Pourmorteza A, Stutman D, Bluemke DA, Lima JAC. Next-Generation Hardware Advances in CT: Cardiac Applications. Radiology 2020;298:3–17.

[12] Schirra CO, Brendel B, Anastasio MA, Roessl E. Spectral CT: a technology primer for contrast agent development. Contrast Media Mol Imaging 2014;9:62–70.

[13] Feldkamp L, Davis LC, Kress J. Practical Cone-Beam Algorithm. J Opt Soc Am 1984;1:612–619.

[14] Smith B. Image Reconstruction from Cone-Beam Projections: Necessary and Sufficient Conditions and Reconstruction Methods. Med Imag, IEEE Trans 1985;4:14–25.

[15] Tuy HK. An Inversion Formula for Cone-Beam Reconstruction. SIAM J Appl Math 1983;43:546–552.

[16] Katsevich A. Theoretically Exact Filtered Backprojection-Type Inversion Algorithm for Spiral CT. SIAM J Appl Math 2002;62: 2012–2026.

[17] Zou Y, Pan X. Exact image reconstruction on PI-lines from minimum data in helical cone-beam CT. Phys Med Biol 2004;49: 941–959.

[18] Yu H, Wang G. Studies on implementation of the Katsevich algorithm for spiral cone-beam CT. J X-Ray Sci Technol 2004;12:97–116.

[19] Lu Y, Zhao J, Wang G. Exact image reconstruction with triple-source saddle-curve cone-beam scanning. Phys Med Biol 2009;54: 2971–2991.

[20] Katsevich A. An improved exact filtered backprojection algorithm for spiral computed tomography. Adv Appl Math 2004;32:681–697.

[21] Holbrook MD, Clark DP, Badea CT. Dual source hybrid spectral micro-CT using an energy-integrating and a photon-counting detector. Phys Med Biol 2020;65:205012.

[22] Orlov S. Theory of three-dimensional reconstruction: 1. Conditions of a complete set of projections. Sov Phys Crystallogr 1975;20:312–314.

[23] Ronaldson JP, Zainon R, Scott NJA, Gieseg SP, Butler AP, Butler PH, et al. Toward quantifying the composition of soft tissues by spectral CT with Medipix3. Med Phys 2012;39:6847–6857.

[24] Persson M, Huber B, Karlsson S, Liu X, Chen H, Xu C, et al. Energy-resolved CT imaging with a photon-counting silicon-strip detector. Phys Med Biol 2014;59:6709.

[25] Yu Z, Leng S, Jorgensen SM, Li Z, Gutjahr R, Chen B, et al. Evaluation of conventional imaging performance in a research whole-body CT system with a photon-counting detector array. Phys Med Biol 2016;61:1572–1595.

[26] Muenzel D, Bar-Ness D, Roessl E, Blevis I, Bartels M, Fingerle AA, et al. Spectral Photon-counting CT: Initial Experience with Dual-Contrast Agent K-Edge Colonography. Radiology 2017;283:723–728.

[27] Si-Mohamed S, Bar-Ness D, Sigovan M, Cormode DP, Coulon P, Coche E, et al. Review of an initial experience with an experimental spectral photon-counting computed tomography system. Nucl Instrum Methods Phys Res, Sect A 2017;873:27–35.

[28] Abadi E, Harrawood B, Rajagopal JR, Sharma S, Kapadia A, Segars WP, et al. Development of a scanner-specific simulation framework for photon-counting computed tomography. Biomed Phys Eng Express 2019:5.

[29] Siewerdsen JH, Waese AM, Moseley DJ, Richard S, Jaffray DA. Spektr: A computational tool for x-ray spectral analysis and imaging system optimization. Med Phys 2004;31:3057–3067.

[30] Yang H, Li M, Koizumi K, Kudo H. Application of Pack and Noo's Cone-Beam Inversion Formula to a Wide Class of Trajectories. 2006 IEEE Nuclear Science Symposium Conference Record; 2006. p. 3471–5.

[31] Zhou W, Bovik AC, Sheikh HR, Simoncelli EP. Image quality assessment: from error visibility to structural similarity. IEEE Trans Image Process 2004;13:600–612.

[32] Rajbhandary PL, Hsieh SS, Pelc NJ. Effect of Spectral Degradation and Spatio-Energy Correlation in X-Ray PCD for Imaging. IEEE Trans Med Imaging 2018;37:1910–1919.

[33] Sidky EY, Pan XC. Image reconstruction in circular cone-beam computed tomography by constrained, total-variation minimization. Phys Med Biol 2008;53:4777–4807.

[34] Kyriakou Y, Kalender WA. Intensity distribution and impact of scatter for dual-source CT. Phys Med Biol 2007;52:6969–6989.

[35] Zhang Z, Zhang X, Hu J, Xu Q, Li M, Wei C, et al. An Optimized K-Edge Signal Extraction Method for K-Edge Decomposition Imaging Using a Photon Counting Detector. Front Phys 2021:8.